Solute effects on dynamics and deformation of emulsion droplets during freezing

Sidhanth Tyagi[1,2], Cécile Monteux[2,3], and Sylvain Deville[4]

[1]*Laboratoire de Synthèse et Fonctionnalisation des Céramiques, UMR 3080*

CNRS/Saint-Gobain CREE, Saint-Gobain Research Provence, Cavaillon, France.

[2]*Sciences et Ingénierie de la Matiére Molle, ESPCI Paris, PSL Research University,*

CNRS, Sorbonne Universités, UPMC Univ Paris 06, Paris, France.

[3]*Global Station for Soft Matter, Global Institution for Collaborative Research and*

Education, Hokkaido University, Sapporo, Japan.

[4]*Université de Lyon, Université Claude Bernard Lyon1, CNRS, Institut Lumière*

Matière, 69622 Villeurbanne, France.

June 25, 2021

Abstract

Soft or rigid particles, suspended in a liquid melt, interact with an advancing solidification front in various industrial and natural processes, such as fabrication of particle-reinforced-composites, growth of crystals, cryopreservation, frost heave, and growth of sea ice. The particle dynamics relative to the front determine the microstructure as well as the functional properties of the solidified material. The previous studies have extensively investigated the interaction of foreign objects with a moving solid-liquid interface in pure melts while in most real-life systems, solutes or surface active impurities are almost always present. Here we study experimentally the interaction of spherical oil droplets with a

1

moving planar ice-water interface, while systematically increasing the surfactant concentration in the bulk liquid, using *in situ* cryo-confocal microscopy. We demonstrate that a small amount of surfactant in the bulk liquid can instigate long-range droplet repulsion, extending over a length scale of 40 to 100 μm, in contrast to the short-range predicted previously ($< 1 \mu m$). We report on the droplet deformation, while they are in contact with the ice-water interface, as a function of the bulk surfactant concentration, the droplet size, and the crystal growth rate. We also depict the dynamic evolution of solute-enriched premelted films ($\approx 5 \mu m$). Our results demonstrate how an increasing concentration of surfactant in the bulk and its subsequent segregation during solidification can dramatically alter the solidification microstructures. We anticipate that our experimental study can serve for the development of theoretical models incorporating solute effects.

Keywords: solidification, solute, droplets, deformation, dynamics

1   Introduction

The interaction of particles with an approaching solid-liquid interface is of special relevance in nature, like frost heave, glacial motion [1], and in engineering sciences, such as food freeze-thaw stability [2], cryopreservation [3, 4], metallurgy [5], and crystal growth [6]. This dynamic problem consists of particles, soft or hard, dispersed in a liquid melt interacting with a solid-liquid interface. The objects can be biological cells in cryopreservation [3, 4], colloids in freeze-casting [7], droplets in food preservation [8], gas bubbles in growth of single crystals [6, 9] and metallurgy [5], or reinforcing particles in material-matrix-composites [10]. The outcome of the particle-interface confrontation determines the solidified microstructure and hence, the functional properties of the solidified material. Thus, it is essential to understand the underlying mechanisms of solidification (or freezing) to forge the required material microstructure. The particle can interact with an advancing solidification interface with diverse outcomes; it can be engulfed instantaneously upon contact, pushed ahead in the remaining liquid by the interface indefinitely, or it may undergo engulfment after being pushed over a certain distance [11].

The dynamics of interaction and spatial distribution of particles are essential features in several material fabrication routes. In particle-reinforced-composites, an instantaneous engulfment in solid phase is desired as it facilitates a homogeneous distribution of the suspended objects [10]. In metallurgy and crystal growth, a continuous repulsion of the impurities by the interface is required to obtain impurity-free-solids [5]. In freeze-casting, a segregation of the colloidal particles by the growing solid enables a porous material structure [7]. The shape of the particle (deformed or undeformed) becomes an equally important processing criterion in applications where soft deformable objects (droplets or bubbles) encounter a moving solid-liquid interface. In cryobiology, utmost care should be taken to avoid physical injury inflicted to the cells from the growing ice crystals [12]. In food preservation, freezing is conducted to conserve the

3

size, shape, and distribution of the dispersed droplets, thereby preserving the original taste and appearance [8]. Thus, numerous interaction scenarios, still poorly understood, can exist during solidification.

The role and concentration of solute in the solidifying liquid is often significant and a dominating factor in determining, amongst others, the shape of the solid-liquid interface in the vicinity of the suspended particles [13–15]. Solutes, render the interfacial curvature concave, thereby promoting engulfment of objects at growth rates lower than those predicted for planar curvatures [16,17]. The solutes can be either desired, like additives (e.g. cryoprotectant used in preservation of biological cells), or be present as an undesired impurity, such as dissolved gases (H_2) in liquid metals or surface active impurities. The segregation of solutes at the interface is instigated by their relatively low solubility in the solid phase and enhanced further by the approaching objects obstructing their diffusion field [13]. This local solute enrichment is of particular importance in understanding the nucleation and growth of macroporosity in solidifying melts [14], studying the constitutional supercooling with formation of premelted films [18,19], and in determining the osmotic stresses acting on a freezing biological cell [4,12] to give a few examples. Moreover, the morphology of a solid-liquid interface (planar, columnar, or dendritic), determined by the magnitude of solute concentration gradient build-up ahead of the growing solid, plays a major role on the final microstructure [13,20].

The study of solidification mechanisms such as the particle dynamics, shape evolution, and the local solute concentration are complex and require *in situ* investigations. The major problem associated with studying solidification *in situ* arises from the need of high space and temporal resolution in conjunction with elevated temperatures especially for metals. For the object dynamics, past studies have formulated a plethora of analytical and numerical models expressing the outcome (engulfment or rejection) of objects interacting at close distances (< 10 nm) with the solid-liquid interface [16,21–24]. The models vary in the mathematical formulation of the features taken into account (e.g. the inclusion

4

of object-melt thermal conductivity mismatch, solute effects etc. . .), while using a similar approach (balance of repulsive and attractive forces between the object and front) to describe the interaction [11]. The study of particle deformation has been of particular interest in the prediction of pore shape evolution during directional solidification of crystals to avoid or control porosity defects. Much of the progress in this domain has been achieved through numerical simulations and post-solidification analysis [25, 26]. *In situ* experimental evidence of solidification dynamics (repulsion or engulfment) and shape modification have been facilitated using transparent analogs (e.g. succinonitrile-acetone) with optical microscopes at ambient temperatures [20, 27] and X-ray transmission microscope at elevated temperatures [14, 28]. However, the volume investigated along with the temporal resolution is limited, while the local solute segregation cannot be visualized. Hence, the tracking of microstructures where objects interact with a solid-liquid interface in the presence of solute effects remains challenging.

In this study, we analyse the interaction of spherical oil droplets with an advancing ice-water interface using *in situ* cryo-confocal microscopy. Our custom solidification setup enables a small temporal resolution (1.7 s) and high spatial resolution (1024×1024 pixels) with laser-induced fluorescence to distinguish the accumulation of a fluorescent water-soluble dye rejected by the ice. We prepare oil-in-water emulsions using microfluidics stabilized with a varying amount of surfactant Tween 80 in the aqueous phase. We further characterise and report on the *in situ* droplet dynamics, droplet deformation, and the role of surfactant on the droplet behaviour.

We investigate the impact of an increasing surfctant concentration on the mechanisms involved at three different stages: droplets in water (water) far from the solidification front, droplets in contact with an approaching solid-liquid interface, and droplets captured in the growing ice. For the droplet-front interaction dynamics, we depict distinct behaviours such as instantaneous engulfment and repulsion-engulfment transition. While confronting a solid-liquid interface, the droplet shape evolution depends on the imposed growth rate and

the surfactant concentration. Furthermore, we show the impact of surfactant on the evolution of premelted films surrounding the oil droplets in ice. Finally, we depict that the three interaction stages are crucial in determining the droplet spatial distribution and shape evolution, and hence, the solidification microstructure.

2 Methods

2.1 Materials

We purchased the oil (propyl benzoate), surfactant (Tween 80), oil fluorophore (Difluoro2-[1-(3,5-dimethyl-2H-pyrrol-2-ylidene-N)ethyl]-3,5-dimethyl-1H-pyrro lato-Nboron), and aqueous fluorophore (Sulforhodamine B) from Sigma-Aldrich. The fluorophores are referred to as BODIPY (incorporated in oil) and SRhB (incorporated in water) in the study. We cycled the deionized water through 0.45 μm Nylon membrane filters (VWR International) to remove traces of impurities and ensure purity of the emulsions prepared. The solidification experiments were conducted to study the interaction of dispersed phase with the ice-water interface. Hence, we prepared oil-in-water emulsions to ensure the dispersed phase remained liquid, while the continuous phase underwent solidification. Thus, we chose propyl benzoate owing to its low melting temperature ($T_m = -51.6^\circ$ C), low solubility in water (0.035 $g/100$ g), and similar density to water ($\rho_{oil} = 1.023$ $g \cdot cm^{-3}$).
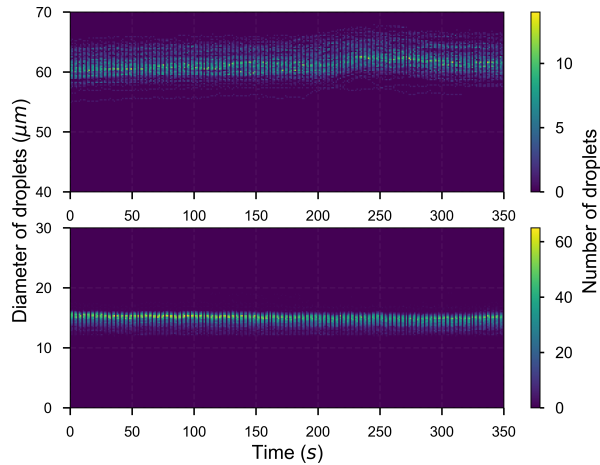
2.2 Sample Preparation

Figure 1: **Diameter of monodisperse droplets with radii (R_1, R_2) of 7.2 ± 0.4 μm and 30.9 ± 1.2 μm respectively, generated using microfluidics.** The size of droplets remained stable during the experimental time-scale, which varied from 15 min to 4 h. © (2020) S. Tyagi *et al.* (10.6084/m9.figshare.14815083) CC BY 4.0 license https://creativecommons.org/licenses/by/4.0/.

We prepared the oil-in-water emulsions using a microfluidic setup, as explained in our previous study [15]. The monodisperse droplets have radii (R_1, R_2) of either 7.2 ± 0.4 μm or 30.9 ± 1.2 μm, as shown in Fig.1. The oil phase consisted of propyl benzoate with 10^{-4} M BODIPY to obtain clear imaging of dispersed droplets at 1% laser power. For the aqueous phase, we used 10^{-5} M SRhB solution, as self-quenching was reported at concentrations above 2×10^{-4} M [29]. We added Tween 80 ($HLB = 15$ [30]), a non-ionic surfactant, to the aqueous phase to stabilise the oil droplets. The surfactant Tween 80 ($cmc = 13 - 15$ $mg \cdot l^{-1}$ [31]) also acts as a solute and hence colligatively depresses the freezing point of solutions, when its concentration increases locally [15]. We prepared three aqueous solutions with 0.01, 0.1, and 1 $wt.\%$ Tween 80 to study the impact of solute concentration on the solidification dynamics and behaviour of oil droplets dispersed in an aqueous phase. The surfactant is added as $wt.\%$ of the aqueous solution to have an equal concentration in all the solutions prepared.

7

¹⁶¹ The concentration of surfactants in the bulk solution at which micelles start

¹⁶² forming is known as the *cmc*. Individual surfactant molecules that are in the

¹⁶³ system but are not part of a micelle are called monomers [32]. At $1wt.\%$ of

¹⁶⁴ Tween 80 in aqueous solution we are $\approx 600\times$ *cmc*. All experiments are therefore

¹⁶⁵ performed above the *cmc* and increasing the surfactant concentration results

¹⁶⁶ in an increase of the number of micelles in solution while the concentration

¹⁶⁷ of surfactant monomers remains approximatively equal to the *cmc*. The oil-

¹⁶⁸ in-water emulsion stabilized by the surfactant is represented schematically in

¹⁶⁹ Fig.2. The presence of micelles at the given concentration was confirmed by

¹⁷⁰ dynamic light scattering (DLS) analysis. A typical micelle size of 9 nm with a

¹⁷¹ corresponding diffusion coefficient of 30 $\mu m^2 \cdot s^{-1}$ at 273 K was obtained from

¹⁷² the DLS analysis. The prepared emulsions were filled through capillarity and

¹⁷³ solidified in a rectangular Hele-Shaw cell (height $=100$ μm and volume $=100$ μl).

¹⁷⁴ We fabricated the Hele-Shaw cell using two glass slides (Menzel, 24×60 mm,

¹⁷⁵ thickness $0.13 - 0.16$ mm), and sealed it with nail-polish at one end to prevent
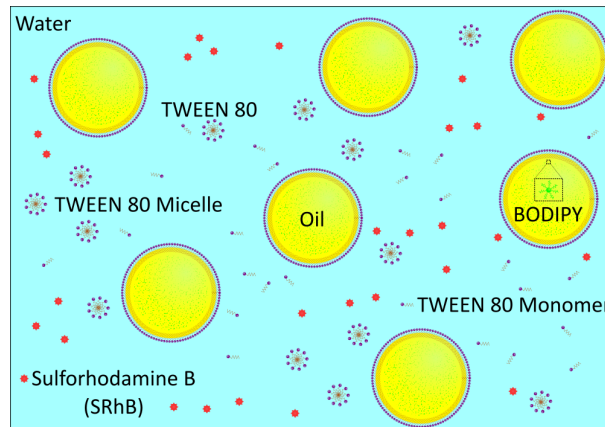
¹⁷⁶ evaporation and leakage.

Figure 2: **Schematic depicting a monodisperse oil-in-water emulsion with the surfactant Tween 80 and fluorophore SRhB added to the aqueous phase (not to scale). The oil phase is incorporated with the fluorophore BODIPY.** The surfactant form micelles. © (2020) S. Tyagi *et al.* (10.6084/m9.figshare.14815083) CC BY 4.0 license https://creativecommons.org/licenses/by/4.0/.

2.3 Imaging & Analysis

We used a Leica TCS SP8 confocal laser scanning microscope (Leica Microsystemes SAS, Germany) equipped with 488 nm (blue), 552 nm (green) lasers and two photodetectors (PMT) for image acquisition. The images were captured for the emission spectra of BODIPY (oil phase) and SRhB (aqueous phase), using a non-immersive objective (Leica HCX PL APO CS 20×) with a working distance of 590 μm. Ice does not fluoresce and hence, we can simultaneously detect three phases (oil droplets, unfrozen aqueous phase, and ice) with two photodetectors. In *2D*, we used the microscope at a scanning speed of 600 Hz, with 1024×1024 $pixels$ for imaging 775×775 μm, resulting in 1.7 s per frame. We used Fiji [33] for image thresholding in conjunction with Python [34] for image and data analysis.
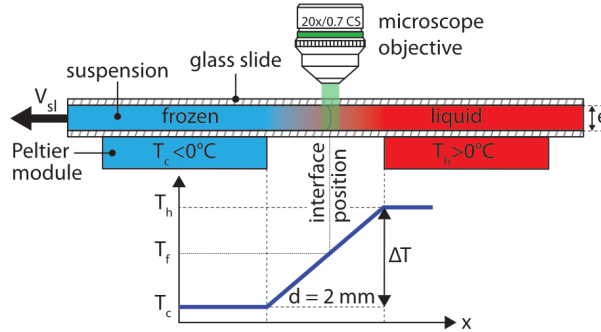
2.4 Freezing Stage

Figure 3: **Cryo-confocal microscope setup to perform *in situ* solidification experiments.** A Hele-Shaw cell containing an oil-in-water emulsion is pulled at a constant velocity (V_{sl}) through a constant linear temperature gradient (G), established by two Peltier elements. In *steady-state*, the solidification interface is at a constant position under the microscope objective. In the sample frame, the interface is moving at a solidification velocity of V_{sl}, imposed by the motor.© (2020) S. Tyagi *et al.* (10.6084/m9.figshare.12046560) CC BY 4.0 license https://creativecommons.org/licenses/by/4.0/.

We conducted unidirectional solidification experiments, translating the sample cell at a constant velocity (V_{sl}) along a constant linear temperature gradient (G)

of $10^4 \ K \cdot m^{-1}$, using the cryo-confocal stage described in detail previously [35]. We imposed the temperature with two Peltier modules, and controlled it with high precision ($< 0.01 \ °C$) using TEC-1122 Dual Thermo Electric Cooling Temperature Controller from Meerstetter Engineering, Switzerland. The Peltier elements were separated by a distance of 2 mm to establish a linear temperature gradient along $\vec{x}$. The *in situ* observation of objects interacting with the solid-liquid interface was achieved using a confocal microscope mounted vertically over the gap (2 mm) between the two Peltier modules, as shown in Fig.3. The solidification interface appears immobile in the frame of observation, however, in the sample frame, a solidifying front at the velocity V_{sl} is advancing in the sample (along $\vec{x}$). We utilised the VT-80 translation stage (Micos Pollux Drive PI, USA) to impose the rate at the which the sample cell is pulled through the temperature gradient. The rate of translation was verified to be in agreement with the measured solidification velocity (V_{sl}), using posterior image analysis ($error < 1 \ \%$). Thus, we can decouple and control independently the solidification velocity (V_{sl}) and the thermal gradient (G) in our system.

We performed the solidification experiments in the velocity range of $1.0 \leq \ V_{sl} \ \leq \ 10.0 \ \mu m \cdot s^{-1}$. We wait for $20-30 \ mins$ to ensure a *steady-state* diffusion controlled regime before starting the acquisition at a given solidification velocity. The time needed for a steady-state to establish scales as $2D/V_{sl}^2 \approx 60 \ s$, where D is the solute diffusion coefficient. We do not expect forced convection in our experiments as they are performed in a closed Hele-Shaw cell of small thickness (100 μm) and at low solidification velocity with a steady linear temperature gradient. The solid-liquid interface is stable over extended time periods ($\approx 4-5 \ hours$) and the interface does not accelerate or decelerate during the solidification experiments. In addition, we do not observe a transient unsteady regime and the interface morphology is stable for the given experimental parameters.

3 Results & Discussions

We performed horizontal solidification experiments by displacing a Hele-Shaw cell, containing an oil-in-water emulsion, in a custom cryo-confocal stage, at a velocity of V_{sl}. A typical *2D* confocal image of a freezing emulsion with the distinct features observed is shown in Fig.4A. The confocal image enables us to distinguish three phases; oil phase in cyan (fluorophore BODIPY), water in colormap viridis (fluorophore SRhB), and a dark ice phase. As solidification progresses, the growing ice phase rejects the dissolved dye, SRhB, owing to its low solubility and hence appears black, which enables us to visualize the solid-liquid interface. In the frame of the ice-water interface, the interface is stationary and the droplets far from the ice-water interface are translated at a velocity V_{sl} toward the ice-water interface. In the frame of the sample, the interface is advancing through the sample at a velocity of V_{sl} along $\vec{x}$ and eventually encounters droplets which velocity, noted U_r (defined in Fig. S2) is indicated in Fig.4A. We also note the premelted films between two ice surfaces as well as around the oil droplets captured in the ice phase, which are due to the rejection of the dye by the ice and subsequent depression of the freezing point.

A typical time-lapse evolution of an isolated oil droplet interacting with the ice-water interface obtained for an oil-in-water emulsion with $1wt.\%$ Tween 80 in the aqueous phase is shown in Fig.4B. The interaction of oil droplets with the solid-liquid interface can be divided in three different stages, which are described below in three different sections. First, we investigate the solidification mechanisms at play when the oil droplets are far from the advancing interface. We investigate the role of an increasing bulk surfactant concentration and the different solidification parameters (growth rate, droplet size) on the droplet dynamics in water ($t < 44\ s$ in Fig.4B). Second, we look into the impact of the approaching solid-liquid interface on the droplet shape upon their mutual contact ($44 \leq t \leq 57\ s$ in Fig.4B). Third, we analyse the droplets captured in ice and report on the evolution of premelted films with the associated ice-water

11

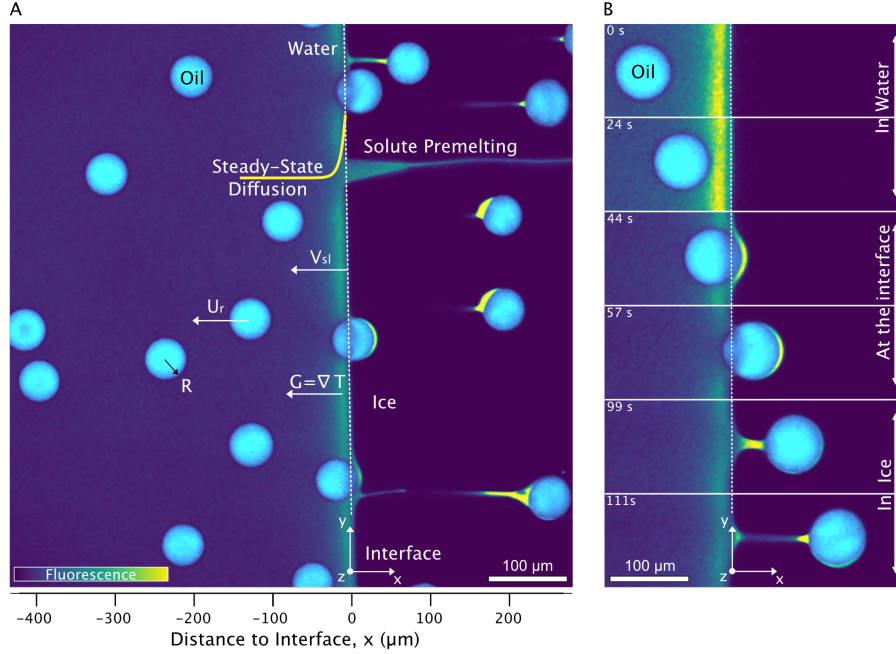meniscus ($99 \leq t \leq 111$ s in Fig.4B).

Figure 4: **2D cryo-confocal image of freezing an oil-in-water emulsion in the presence of** $1wt.\%$ **Tween 80 in the aqueous phase.** (A) Typical features observed for a planar growth at $V_{sl} = 2$ $\mu m \cdot s^{-1}$ (B) Time-lapse evolution of an oil droplet encountering an approaching solid-liquid interface with three distinct regimes of interaction at $V_{sl} = 2$ $\mu m \cdot s^{-1}$. Ice is in black, oil droplets in cyan, and the aqueous phase is in colormap viridis (fluorescence bar). $©$ (2020) S. Tyagi *et al.* (10.6084/m9.figshare.14815083) CC BY 4.0 license https://creativecommons.org/licenses/by/4.0/.

3.1 Droplets in water

We track the trajectories of the oil droplets which enables us to deduce the isolated droplet velocity U_r in the sample frame (see details in Fig. S1 and S2). Our Hele-Shaw cell of length 4 cm facilitates an acquisition of $50 - -400$ isolated droplet velocities and we deduce the mean droplet velocity as $\overline{U} = \langle U_r \rangle$ (The python script employed can be found in a previous study [19]). A positive magnitude of $\overline{U}$ implies that the droplets are repelled or pushed by the moving ice-water interface towards the remaining liquid.

In Fig.5, we present the mean droplet velocity, $\overline{U}$, with the distance to

²⁵⁹ interface for an interface velocity of V_{sl} of $3 \ \mu m \cdot s^{-1}$. We define the distance to

²⁶⁰ interface as $0 \ \mu m$ when the front edge of the droplet comes in contact with the

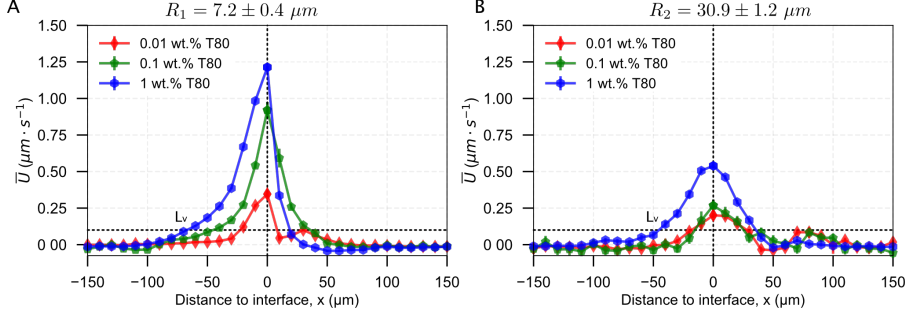²⁶¹ absolute detected position of the ice-water interface.

Figure 5: **Droplet dynamics in presence of** 0.01, 0.1, **and** $1wt.\%$ **solute in solution, deduced from the droplet trajectories at** $V_{sl} = 3 \ \mu m \cdot s^{-1}$. Mean droplet velocity versus distance to interface for (A) $R_1 = 7.2 \pm 0.4 \ \mu m$ and (B) $R_2 = 30.9 \pm 1.2 \ \mu m$. The droplets accelerate as the solidification front approaches, and decelerate as they are engulfed into the ice. © (2020) S. Tyagi *et al.* (10.6084/m9.figshare.14815083) CC BY 4.0 license https://creativecommons.org/licenses/by/4.0/.

²⁶² At large distances from the interface, larger than $100 \ \mu m$ the droplets in

²⁶³ water are unperturbed and their mean velocity $\overline{U}$ in the sample frame is zero.

²⁶⁴ As they get closer to the interface, they start getting repelled. The mean droplet

²⁶⁵ velocity ($\overline{U}$) increases and exhibits a maximum (U_{max}), when the leading edge

²⁶⁶ of the droplets coincides with the initial position of the growing crystal. We note

²⁶⁷ that the droplet velocity $\overline{U}$ is lower than V_{sl}, which means that the droplets are

²⁶⁸ finally captured in ice after a typical time, called interaction time (defined in

²⁶⁹ Fig. S1), which is discussed later. As the droplets are captured in ice, their

²⁷⁰ velocity $\overline{U}$ returns to zero. As shown in Fig.5, $\overline{U}$ decreases for a larger droplet

²⁷¹ size, while it increases with an increasing surfactant concentration.

²⁷² In Fig.6, we report the evolution of the maximum velocity U_{max} with the

²⁷³ surfactant concentration, the droplet size, and the solid liquid interface velocity

²⁷⁴ V_{sl}. Similar to $\overline{U}$, we observe an increase of U_{max} with an increasing surfactant

²⁷⁵ concentration and that the larger R_2 droplets get pushed away from the growing

²⁷⁶ solid at lower velocities as compared to the smaller R_1 droplets. Furthermore,

13

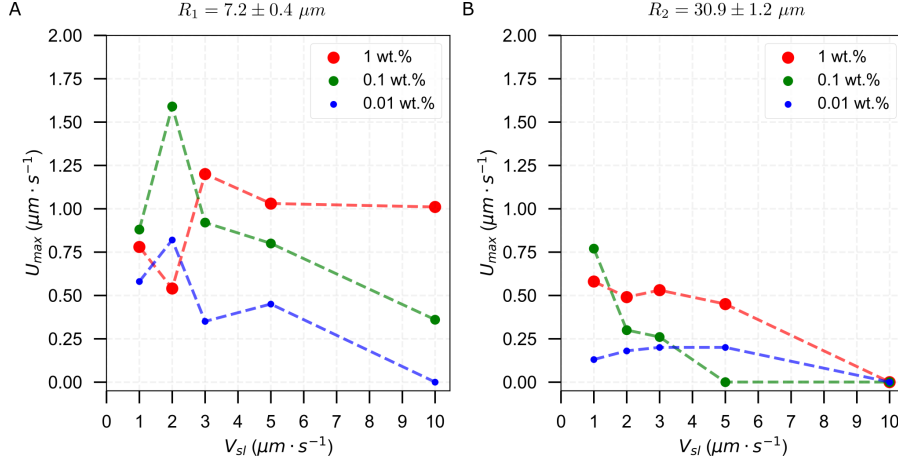increasing V_{sl} leads to a decrease of the U_{max}.

Figure 6: **Maximum mean droplet velocity (U_{max}) when the droplet front edge coincides with the ice-water interface (distance to interface = 0 μm) for (A)** $R_1 = 7.2 \pm 0.4 \ \mu m$ **and (B)** $R_2 = 30.9 \pm 1.2 \ \mu m$. In general, the magnitude of U_{max} is greater for higher surfactant concentrations and smaller droplet sizes. An increasing growth rate V_{sl} as well as droplet radius promote a smaller magnitude of U_{max}. The dotted lines are for visualization and do no represent an extrapolation of the results denoted by the circular markers. © (2020) S. Tyagi *et al.* (10.6084/m9.figshare.14815083) CC BY 4.0 license https://creativecommons.org/licenses/by/4.0/.
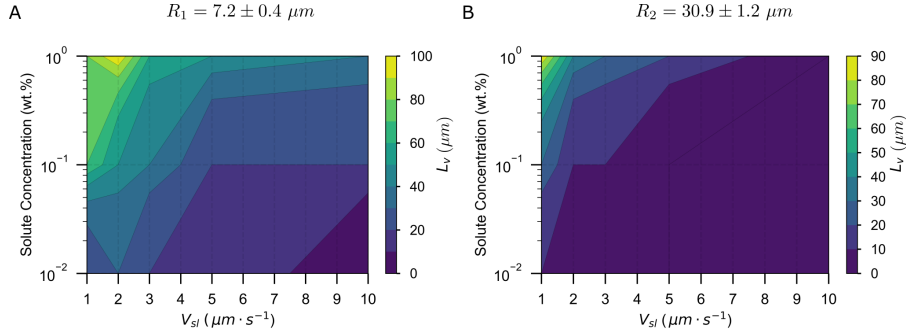

Figure 7: **Characteristic length scale L_v in the plane of Solute Concentration ($wt.\%$) versus Solidification Velocity (V_{sl}).** Contour plots denoting the magnitude of L_v for (A) $R_1 = 7.2 \pm 0.4 \ \mu m$ and (B) $R_2 = 30.9 \pm 1.2 \ \mu m$. Each contour line denotes a constant magnitude of L_v equivalent to the value shown on the calibration bar. The distance L_v, where droplets in water start getting repelled by the interface, increases significantly with the solute concentration, while it decreases with an increasing growth rate. © (2020) S. Tyagi *et al.* (10.6084/m9.figshare.14815083) CC BY 4.0 license https://creativecommons.org/licenses/by/4.0/.

278 From the evolution of $\overline{U}$ with the distance to the interface, we define a char-
279 acteristic length scale, L_v, corresponding to the distance at which the droplets
280 attain a mean velocity ($\overline{U}$) of 0.1 $\mu m \cdot s^{-1}$, which is shown in Fig.7. This distance
281 corresponds to the range of interaction between the droplets and the interface.
282 We find that the droplets get repelled over distances ranging between 10 and
283 100 μm, often larger than their diameter, especially for the largest surfactant
284 concentrations. Smaller droplets with radius R_1 are repelled at greater distances
285 from the interface as compared to the larger R_2 droplets. Increasing the growth
286 rate decreases the characteristic distance L_v.

287 We also depict in Fig.8 the interaction time τ (defined in SI), which repre-
288 sents the time during which the velocity of the droplets is different from zero
289 before and after crossing the interface. In general, we notice that the interaction
290 time diminishes with an increasing solidification velocity (V_{sl}) and reduces to
291 zero at higher growth rates ($V_{sl} \geq 5 \ \mu m \cdot s^{-1}$), independent of the surfactant
292 concentration. An interaction time of 0 s implies that the droplets get engulfed
293 into the ice instantaneously and hence, are not repelled by the advancing solid-
294 liquid interface. In contrast, the interaction time increases strongly with the
295 surfactant concentration at relatively lower growth rates ($V_{sl} \leq 3 \ \mu m \cdot s^{-1}$).

296 In Fig.9 we present the droplet displacement δ due to their repulsion by the
297 front (defined in Fig. S1), which represents the distance moved by the droplets
298 during the interaction time. We again observe that increasing the surfactant
299 concentration leads to higher displacements while increasing the growth rate
300 leads to a lower displacement.

301 The results described so far emphasize that an increasing amount of surfac-
302 tant induces a repulsion of the droplets by the interface over large distances,
303 of the order ten to a hundred of microns away from the interface and that the
304 droplet dynamics is influenced by the bulk surfactant concentration, the growth
305 rate and the droplet size. These three parameters control the local gradient of
306 surfactant concentration close to the solidification front. Indeed the surfactant
307 concentration close to the solid-liquid interface is higher as compared to the
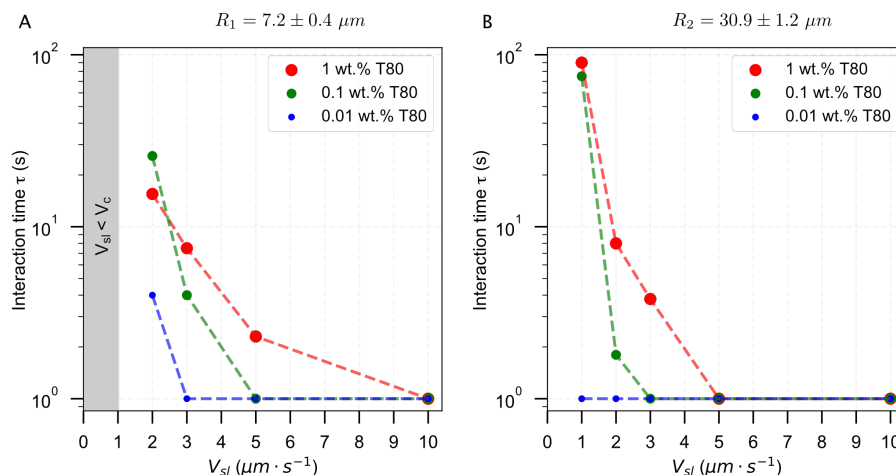
15

Figure 8: **Interaction time for oil droplets dispersed in water at three distinct solute concentrations.** Plot of characteristic interaction time for (A) $R_1 = 7.2 \pm 0.4 \ \mu m$ and (B) $R_2 = 30.9 \pm 1.2 \ \mu m$. Droplets tend to interact or feel the presence of an approaching ice-water interface during 10 to 100 s at high solute concentrations ($\geq 0.1 \ wt.\%$) and low growth rates ($\leq 5 \ \mu m \cdot s^{-1}$). The dotted lines are for visualization and do no represent an extrapolation of the results denoted by the circular markers. © (2020) S. Tyagi *et al.* (10.6084/m9.figshare.14815083) CC BY 4.0 license https://creativecommons.org/licenses/by/4.0/.

³⁰⁸ bulk concentration far from the interface because of its low solubility in ice.

³⁰⁹ For *steady-state* planar growth, the concentration field of rejected solutes in the

³¹⁰ remaining liquid writes

$$C_L = C_0 + C_0 \left(\frac{1 - K_0}{K_0} \right) exp \left[\frac{-V_{sl}}{D} |x| \right] \tag{1}$$

³¹¹ where C_L is the solute concentration at a distance x from the interface, C_0

³¹² is the bulk solute concentration in the liquid far from the interface, D is the

³¹³ solute diffusion coefficient and K_0, the partition coefficient defined as the ratio

³¹⁴ of surfactant concentration in the solid phase to the one in the liquid [36].

³¹⁵ In a previous article [19], we suggested that the displacement of the droplets

³¹⁶ is caused by surfactant concentration gradients close to the ice-water interface,

³¹⁷ possibly through a phenomenon called diffusiophoresis [37]. Diffusiophoresis

³¹⁸ is provoked by solute concentration gradients and can lead to displacement of
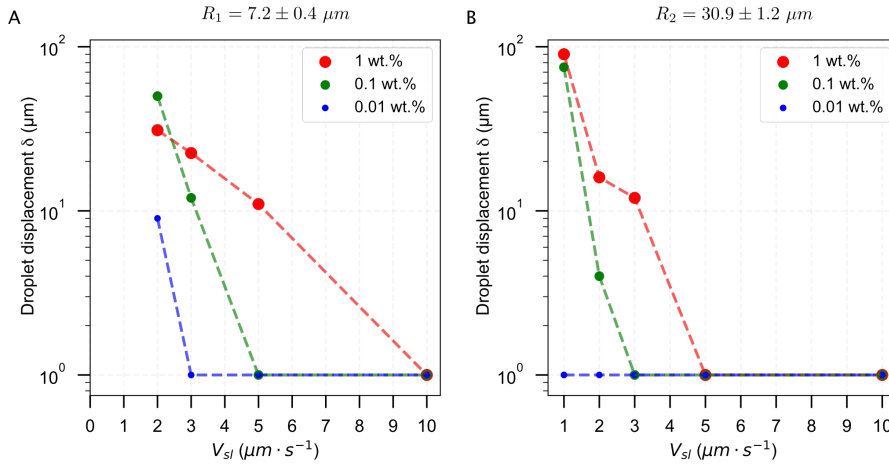
Figure 9: **Displacement of oil droplets dispersed in water at three distinct solute concentrations, while interacting with the ice-water interface.** Plot of droplet displacement for (A) $R_1 = 7.2 \pm 0.4 \ \mu m$ and (B) $R_2 = 30.9 \pm 1.2 \ \mu m$. The interaction of droplets with an advancing ice-water interface can displace them by increasing distances ($\geq 10 \ \mu m$) owing to a high amount of surfactant ($\geq 0.1 \ wt.\%$) in the bulk solution. The dotted lines are for visualization and do no represent an extrapolation of the results denoted by the circular markers. © (2020) S. Tyagi *et al.* (10.6084/m9.figshare.14815083) CC BY 4.0 license https://creativecommons.org/licenses/by/4.0/.

³¹⁹ micrometric particles with velocities of the order of a few micron per second,

³²⁰ comparable to the droplet velocities that we measure in our study. From Eq. (1),

³²¹ it is expected that the local gradient of surfactant concentration spans over a

³²² typical distance $L_d = D/V_{sl}$ [36]. Hence an increasing growth rate (V_{sl}) will de-

³²³ crease the distance at which the solute field can be perceived by the droplets and

³²⁴ can qualitatively account for the decreasing values of L_v measured (see Fig.7)

³²⁵ at high growth rates ($V_{sl} \geq 5 \ \mu m \cdot s^{-1}$). Moreover the concentration gradient

³²⁶ $C_L - C_0$ depends linearly on C_0 which can possibly account for the strong influ-

³²⁷ ence of the surfactant concentration on the droplet displacement. We note that

³²⁸ diffusiophoretic displacements of particles have been studied theoretically and

³²⁹ experimentally for simple solutes such as ionic salts, dissolved gas or charged

³³⁰ surfactants such as Sodium dodecylSulfate [37–40] but was never reported for

³³¹ non-ionic species.

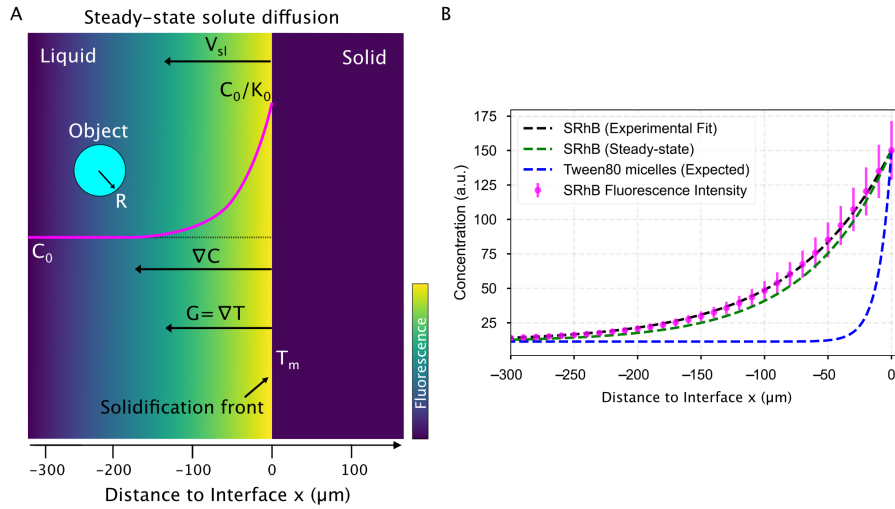³³² To further study the influence of the surfactant concentration gradients on

17

Figure 10: **Solute rejected by the growing solid phase and segregated at the solid-liquid interface during *steady-state* directional solidification.** (A) Model sketch depicting the concentration profile evolution of a solute (in magenta) in the remaining liquid, rejected by a solidification front advancing at V_{sl}, during *steady-state* planar growth. (B) Mean fluorescence intensity (magenta) of SRhB, acquired using a confocal microscope, is fit with a theoretical diffusion-type exponential (black line). The predicted *steady-state* diffusion of SRhB (green line), using the model from Tiller *et al.* [36], corresponds closely to the experimental data fit. A *steady-state* planar growth is thus verified. The corresponding *steady-state* diffusion profile of Tween 80 micelles (blue) shows a significant difference in length scales over which the two molecules (SRhB and Tween 80) diffuse. All data presented was recorded for a growth rate of $3 \ \mu m \cdot s^{-1}$. © (2020) S. Tyagi *et al.* (10.6084/m9.figshare.14815083) CC BY 4.0 license https://creativecommons.org/licenses/by/4.0/.

the droplet dynamics, it would be useful to measure *in situ* the surfactant concentration close to the front. However Tween 80 does not fluoresce, hence we cannot measure its concentration profile. However it is in principle possible to predict it from Equation 1 provided a steady state regime is reached in our experiments. Therefore we examine the validity of Equation 1 by recording the fluorescence intensity of the dye, SRhB, which can be obtained easily with the confocal microscope (see Fig.10A). The concentration profile of SRhB rejected by the ice-water interface, deduced from the fluorescence intensity profile for a growth rate of $3 \ \mu m \cdot s^{-1}$ is given in Fig.10B. At $3 \ \mu m \cdot s^{-1}$, the concentration profile obtained is in agreement with the *steady-state* diffusion profile predicted

18

from Eq.1 (see Fig.10B). However we note that the *steady-state* approximation is not valid at higher velocities (not shown) probably because constitutional undercooling modifies the local temperature of the front hence the diffusion coefficient of the dye.

Interestingly, we see from Fig.10B which is obtained for a velocity of 3 $\mu m \cdot s^{-1}$, that the distance at which the dye concentration profile starts increasing is of the order of 150 μm. This value is much higher than the typical distance L_v over which both the large and small droplets get repelled from the interface at the same velocity, ranging between 40 and 80 μm depending on the surfactant concentration and the droplet size. As the surfactant monomers and the dye have the same diffusion coefficient, we would expect that the distance L_d is similar for both species.

To account for the discrepancy between the measured values of L_v and the theoretical $L_d = D/V_{sl}$, one may suggest that the droplet dynamics may be controlled by the concentration gradient of surfactant micelles, which diffusion coefficient is lower than that of the monomers and for which we expect a lower value of L_d. Using DLS, we measured the diffusion coefficient of the micelles and calculated the corresponding concentration profile using Eq.1. As shown in Fig.10B, at a growth rate of 3 $\mu m \cdot s^{-1}$, we obtain a typical distance L_d of 10 μm, which is lower than the distance L_v measured experimentally at this growth rate. Hence it turns out that the experimentally measured value of L_v ranges between the L_d values calculated either for the surfactant micelles or for the monomers. However we note that the monomer and micelle concentration profiles close to ice-water front depends on the exchange dynamics between the surfactants and the micelles, hence may not be at equilibrium.

3.2 Droplets at the interface

We now focus on the behaviour of droplets when they come in contact (distance to interface = 0 μm) with the solid-liquid interface. We observe three typical behaviours of oil droplets as they encounter an approaching front, as shown
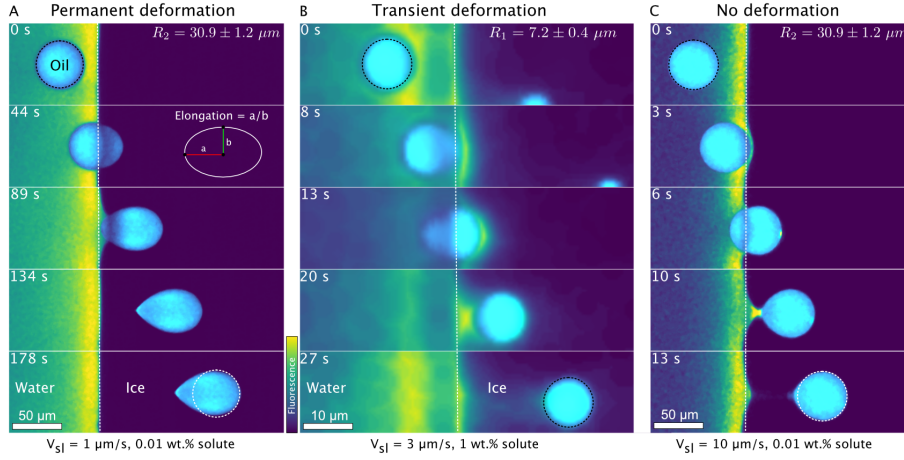
Figure 11: **Typical time-lapse montage depicting the three types of deformation behaviour of oil droplets while undergoing directional planar front solidification.** (A) The droplets elongate at the ice-water interface and remain deformed in the ice phase, scale bar $= 50~\mu m$ (B) The droplets deform in a transient manner ($t = 13~s$) at the ice-water interface and recover their shape as they are captured by the growing ice phase, scale bar $= 10~\mu m$ (C) The droplets do not undergo deformation and preserve their shape during their interaction and further engulfment in the growing crystal. Scale bar $= 50~\mu m$. Oil is in cyan, water is in colormap viridis (fluorescence bar), and ice is in black. $^{©}$ (2020) S. Tyagi *et al.* (10.6084/m9.figshare.14815083) CC BY 4.0 license https://creativecommons.org/licenses/by/4.0/.

in Fig.11. The droplets can elongate permanently as they get engulfed in the growing ice (Fig.11A), the droplets may deform transiently ($t = 13~s$) at the ice-water interface and subsequently relax to their original spherical shape as they move further into the ice phase (Fig.11B), or the droplets remain mostly spherical during their engulfment by the growing crystal (Fig.11C). We notice that the deformation behaviour depends on the droplet size R, the imposed growth rate V_{sl}, and the bulk surfactant concentration. Therefore, we need to systematically study the effect of these solidification parameters to understand the different types of deformation observed.

The droplet deformation is estimated from the analysis of *2D* shape elongation, as shown in the schematic in Fig.11A, taking the ratio of droplet diameters along $\vec{x}$ and $\vec{y}$. In Fig.12, we depict the mean elongation profiles calculated for 50 to 400 (depending on R and V_{sl}) droplet interactions in 0.01 *wt.%* and 1 *wt.%*

20

solute solution at varying growth rates for two different droplet sizes (R_1, R_2).
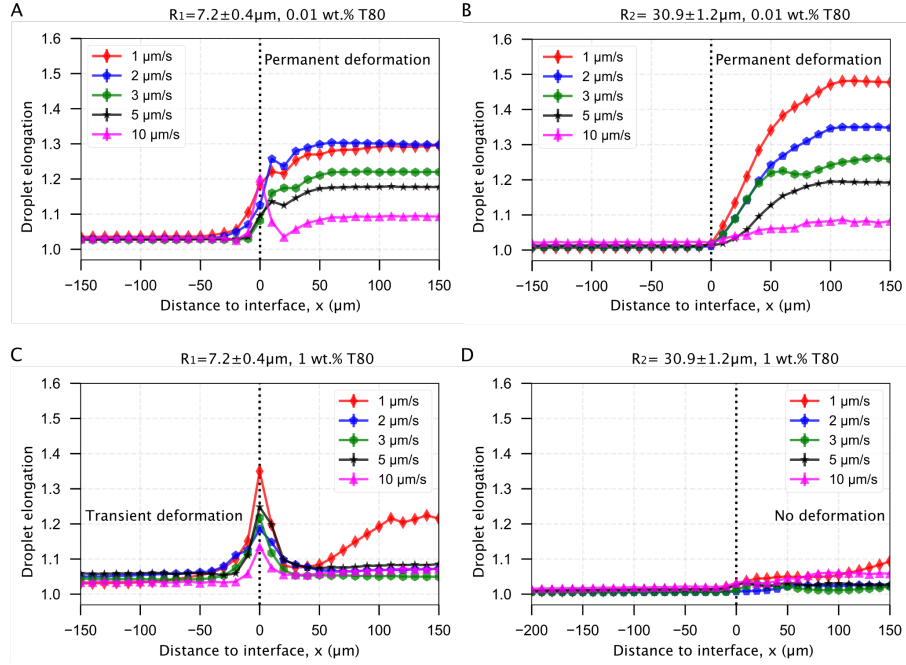

Figure 12: **Mean elongation profiles for oil droplets encountering an approaching ice-water interface.** Planar solidification front induced permanent deformation of oil droplets dispersed in a solution with (A,B) 0.01 $wt.\%$ solute concentration having a size of (A) $R_1 = 7.2 \pm 0.4$ μm (B) $R_2 = 30.9 \pm 1.2$ μm. The transient and no deformation regimes for droplets in (C,D) 1 $wt.\%$ solute concentration having a size of (C) $R_1 = 7.2 \pm 0.4$ μm (D) $R_2 = 30.9 \pm 1.2$ μm. © (2020) S. Tyagi *et al.* (10.6084/m9.figshare.14815083) CC BY 4.0 license https://creativecommons.org/licenses/by/4.0/.

We observe from Fig.12A and Fig.12B that the droplets undergo permanent elongation for the two droplet sizes (R_1, R_2), when the bulk surfactant concentration is 0.01 $wt.\%$. The elongation is ≈ 1.0, representing a circle, when the droplets are in the remaining liquid far from the interface. The droplets start getting elongated as their front edge touches the interface (distance $= 0$ μm) and their shape transforms into an ellipse (elongation > 1.0). The droplet deformation evolves further and reaches a constant magnitude when the front edge is located at a distance of $2R \times Elongation$. Once the droplets are completely engulfed in the ice, their shape does not evolve any more (Fig.12A,B). Interestingly, we notice that the elongation reduces with an increasing growth rate for

both the droplet sizes investigated. However, the maximum elongation for the smaller R_1 droplets is lower as compared to the larger R_2 droplets at the given 0.01 $wt.\%$ solute concentration.

In Fig.12C, we report the transient deformation of the oil droplets as they confront the ice-water interface with 1 $wt.\%$ bulk solute concentration. Here, the oil droplets undergo elongation at the interface (distance $=0$ μm) but eventually recover their shape as they are completely engulfed in the ice. In contrast, from Fig.12D we notice that the larger R_2 droplets do not undergo any type of deformation at the same solute concentration of 1 $wt.\%$. Hence, the elongation profile of R_2 droplets remains unmodified during the droplet-interface confrontation.

We deduce from these observations that the droplets confronting an approaching interface have distinct behaviours depending on the concentration of solute in the bulk solution. In particular, an increasing solute concentration tends to decrease the droplet elongation significantly.

Several experimental and theoretical studies devoted to the shape of bubbles during solidification in the absence of surfactant can be found in the literature [41–43]. Highly elongated bubbles along with the formation of a highly curved tip at the bubble-ice interface were observed [41, 42] and are controlled by the contact angle between the bubbles and the ice-water interface [43]. In the case of the low surfactant concentrations, we see from Fig.11A that the contact angle between the droplets and the ice-water interface remains close to 90° during engulfment, similarly to bubbles, because of the weak thermal flux in the droplets owed to their low thermal conductivity in comparison to water [44]. This results in tear-shaped drops which are very similar to those reported in the literature for bubbles.

At higher surfactant concentration we observe much lower elongations. According to Eq.1, an increasing bulk solute concentration (C_0) implies a higher concentration of the solute segregated (C_0/K_0) at the solid-liquid interface. The segregation of solute is further enhanced owing to an obstruction of their diffu-

₄₂₆ sion field by the droplets in the vicinity of the solid-liquid interface [13,45]. The

₄₂₇ segregated solute, trapped in the layer between the droplet and the interface,

₄₂₈ induces solute premelting [46, 47] (Fig.4B at $t = 44$ s, Fig.11B at $t = 8$ s, in

₄₂₉ Fig.11C at $t = 3$ s) which in turn causes a lowering of the equilibrium melt-

₄₃₀ ing temperature of water. Therefore these premelted films are stable below the

₄₃₁ solid's bulk melting temperature, T_m and the thickness of the premelted films

₄₃₂ increases with the solute concentration [18,46]. As a premelting film interca-

₄₃₃ lates between the droplets and the solid liquid interface, the situation is very

₄₃₄ different from the literature studies discussed above as no finite contact angle

₄₃₅ between the drops and the interface can be defined. Here we suggest that the

₄₃₆ liquid-liquid interfacial tension between the droplet and the premelting film fa-

₄₃₇ vors spherical shapes to minimize the interfacial area. Interestingly we note that

₄₃₈ the effect of size is different at low and high surfactant concentrations. At low

₄₃₉ surfactant concentrations, smaller droplets undergo a lower deformation, prob-

₄₄₀ ably because of a higher capillary pressure inside the drops that opposes the

₄₄₁ deformation. At opposite, for large surfactant concentrations, smaller droplets

₄₄₂ present a transient deformation, while larger droplets remain mostly spheri-

₄₄₃ cal. This effect may be linked to the stronger segregation of solute in the films

₄₄₄ between the droplets and the ice in the case of larger films.

₄₄₅ 3.3 Droplets in Ice

₄₄₆ We have discussed so far the dynamics and consequences of oil droplets interact-

₄₄₇ ing with an approaching ice-water interface. In the last section, we investigate

₄₄₈ the fate of droplets after their engulfment by the ice front.

₄₄₉ At 1 $wt.\%$ solute in the aqueous solution, at a growth rate of 1 $\mu m \cdot s^{-1}$, the

₄₅₀ droplets undergo an elongation process after engulfment whereby the two radii,

₄₅₁ along $\vec{x}$ and $\vec{y}$, are stretched in magnitude as the droplets progress further in

₄₅₂ ice. This means that the droplets flatten in the z direction as they are engulfed

₄₅₃ in the ice. We depict this phenomenon with a time-lapse montage, highlighting

₄₅₄ the deformation, in Fig.13. Interestingly, we observe this phenomenon only at
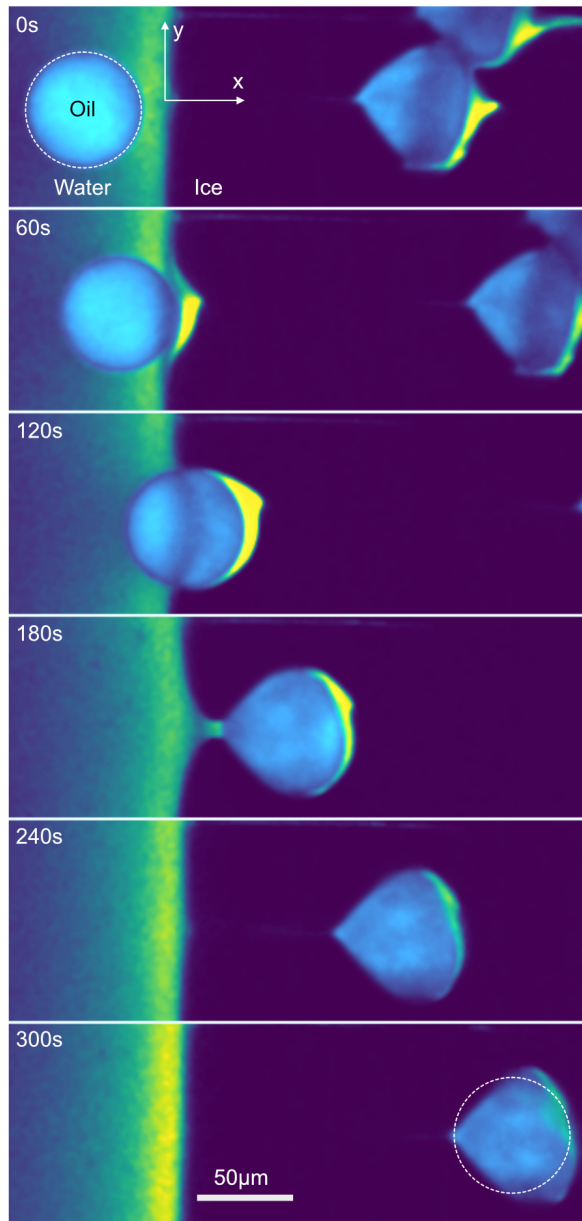
Figure 13: **Crushing of oil droplets during their engulfment in ice at a growth rate of** $V_{sl} = 1 \ \mu m \cdot s^{-1}$ **with** $1 \ wt\%$ **solute in solution.** $R_2 = 30.9 \pm 1.2 \ \mu m$. Typical time-lapse montage depicting the crushing of an oil droplet, scale bar = 50 μm. The dashed circle indicate the shape of the droplet before encapsulation. Note that in the crushing regime, the droplets are elongated in a direction parallel to the front, unlike in the other regimes (elongation perpendicular to the front). © (2020) S. Tyagi *et al.* (10.6084/m9.figshare.14815083) CC BY 4.0 license https://creativecommons.org/licenses/by/4.0/.

24

⁴⁵⁵ a growth rate of $1 \ \mu m \cdot s^{-1}$ in the presence of 1 $wt.\%$ bulk solute concentration

⁴⁵⁶ for both droplets radii R1 and R2.

⁴⁵⁷ We currently have no definitive explanations for this behavior. One possibil-

⁴⁵⁸ ity could be that the shape of the water/ice meniscus in these conditions (curved

⁴⁵⁹ meniscus) may favor entrapment and flattening of the droplets between the ice

⁴⁶⁰ and the glass surface. However, this particular point would deserve additional

⁴⁶¹ experiments, in particular in 3D, which are beyond the scope of the current

⁴⁶² study.

⁴⁶³ Furthermore we note that once the droplets are trapped in the ice, we do

⁴⁶⁴ not observe any thermal regelation, i.e the droplets do not manifest any motion

⁴⁶⁵ relative to the ice. Moreover the liquid layer between the droplet from the

⁴⁶⁶ growing solid decreases in thickness as the droplets move along the temperature

⁴⁶⁷ gradient in ice towards an increasing undercooling ($\Delta T = T_m - T$, where T is

⁴⁶⁸ the temperature of the substrate) [1]. The study of particle migration in ice is an

⁴⁶⁹ important topic of research to understand frost heave, glacier motion, and ice-

⁴⁷⁰ core dating among other technological applications [1]. Recent studies suggest

⁴⁷¹ that the presence of impurities or solutes tend to accelerate the *regelation* of

⁴⁷² trapped particles in ice. Typical migration velocities of $0.1 \ \mu m \cdot s^{-1}$ at ΔT of 1 K

⁴⁷³ have been reported for micron sized particles in the presence of impurities [48].

⁴⁷⁴ Another recent study highlights the major impact of impurities on the rapid

⁴⁷⁵ displacement (0.5 cm) over small time scales (120 s) of 1 μm silicon particles

⁴⁷⁶ trapped in ice [49]. The objects investigated here are 1 order of magnitude (or

⁴⁷⁷ more) larger, which could explain why no regelation was observed. The use of

⁴⁷⁸ cryo-confocal microscopy with the ability to image the solute segregation has

⁴⁷⁹ a promising prospect for investigating such mechanisms. We believe the high

⁴⁸⁰ space and temporal resolution can be used effectively to resolve the dynamics

⁴⁸¹ of individual colloidal particles to gain further insight into *regelation*.

4 Conclusions

In the first section, we have investigated the role of solutes on the dynamics of freezing oil droplets using *in situ* cryo-confocal microscopy. We have reported on the significant magnitude of droplet-front interaction time and the resulting droplet displacement owing to the solute effects. We believe this can be an important criterion for controlling the spatial distribution of objects, especially in multiple object scenarios. The control of the material microstructure has been a topic of interest in alloy solidification (especially in particle-reinforced-composites) and for impurity control in castings and single crystal growth. The object dynamics and impact of solute (or impurity) are still complex to quantify as the observation of solidification *in situ* remains challenging. We have tried to advance towards an *in situ* quantification of the solute mechanisms at play and further work is required to correlate the dye fluorescence intensity to the absolute solute concentration gradient. The latter can be useful in predicting thermal convection and non *steady-state* solidification regimes.

In the second section, we have shown that the deformation of droplets at the ice-water interface depends strongly on the growth rate (V_{sl}) and the corresponding bulk solute concentration (C_0). Furthermore, the addition of solute increases the thickness of the observable premelted films, which appears to act as a protection mechanism against the interface initiated droplet deformation. The local solute environment and deformation are two important criterion for cryopreservation in particular. In cryobiology, the excess of solute causes severe osmotic stresses that can instigate cell membrane rupture and hence, cryoinjury to cells and tissues [4, 12]. In food engineering, alterations to the continuous phase concentration or to the shape and size of dispersed droplets is detrimental to the freeze-thaw stability of consumable emulsions [8]. Hence, a complete understanding of the solute redistribution mechanisms along with the associated object deformation at the corresponding freezing conditions is desired. Our multi-dimensional approach highlights the importance of different solidifi-

26

cation parameters and the ubiquitous role of solute in dominating the various aspects of object deformation behaviour. Further work is required to accurately estimate the direction and magnitude of forces at the origin of the observed deformation.

In conclusion, we report that the oil droplets undergoing directional solidification feel the impact of solute at every stage, from being in the liquid phase to getting captured by the growing ice-water interface. The solute plays an important role in determining the droplet shape (deformed or not), droplet behaviour (engulfment or rejection), and eventually the droplet spatial distribution. To predict the solidified microstructure, an understanding of the several in-situ mechanisms at play is therefore indispensable. The use of rapid cryo-confocal microscopy facilitates an *in situ* investigation and quantification of solidification mechanisms with visualization of the local solute segregation. To represent the observations in real-life systems, we need to explore models incorporating interaction dynamics and object behaviour with solute effects. Current theories do not encompass all the factors required for explaining the long-range solute effects on the objects during solidification. We hope our experimental data can serve to improve the existing theoretical models. Finally, we suggest that the freezing of oil-in-water emulsions may serve as an analogue for studying the *in situ* interaction of foreign objects with an advancing solid-liquid interface in the presence of solute effects.

Acknowledgements

Author contributions

S.D. and C.M. designed and supervised the project, S.D, C.M. and S.T. designed the experiments, S.T. carried out the confocal microscopy, S.T., C.M. and S.D. analyzed the data. All authors discussed the results and implications and wrote the manuscript.

Corresponding Authors

Correspondence should be sent to Cécile Monteux (Cecile.Monteux@espci.fr) and Sylvain Deville (sylvain.deville@univ-lyon1.fr)

Conflict of interest

The authors declare no conflict of interest.

Availability of materials and data

The datasets generated during and/or analysed during the current study are available from the corresponding author on reasonable request.

References

[1] J. G. Dash, A. W. Rempel, and J. S. Wettlaufer. The physics of pre-melted ice and its geophysical consequences. *Reviews of Modern Physics*, 78(3):695–741, 2006.

[2] M Shafiur Rahman. *Handbook of food preservation.* CRC press, 2007.

[3] VL Bronstein, YA Itkin, and GS Ishkov. Rejection and capture of cells by ice crystals on freezing aqueous solutions. *Journal of Crystal Growth*, 52:345–349, 1981.

[4] C Körber. Phenomena at the advancing ice-liquid interface: solutes, particles and biological cells. *Quarterly reviews of biophysics*, 21:229–298, 1988.

[5] Lifeng Zhang. Nucleation, growth, transport, and entrapment of inclusions during steel casting. *Jom*, 65(9):1138–1144, 2013.

[6] H Li, EA Ghezal, A Nehari, G Alombert-Goget, A Brenier, and K Lebbou. Bubbles defects distribution in sapphire bulk crystals grown by czochralski technique. *Optical Materials*, 35(5):1071–1076, 2013.

[7] Sylvain Deville. Freeze-casting of porous ceramics: a review of current achievements and issues. *Advanced Engineering Materials*, 10(3):155–169, 2008.

[8] Supratim Ghosh and John N Coupland. Factors affecting the freeze–thaw stability of emulsions. *Food Hydrocolloids*, 22(1):105–111, 2008.

[9] OM Bunoiu, Th Duffar, and I Nicoara. Gas bubbles in shaped sapphire. *Progress in crystal growth and characterization of materials*, 56(3-4):123–145, 2010.

[10] D. Shangguan, S. Ahuja, and D. M. Stefanescu. An analytical model for the interaction between an insoluble particle and an advancing solid/liquid interface. *Metallurgical Transactions A*, 23(2):669–680, 1992.

[11] R. Asthana and S. N. Tewari. The engulfment of foreign particles by a freezing interface. *Journal of Materials Science*, 28(20):5414–5425, 1993.

[12] Gregory M. Fahy. The relevance of cryoprotectant "toxicity" to cryobiology. *Cryobiology*, 23(1):1–13, 1986.

[13] J. K. Kim and P. K. Rohatgi. The effect of the diffusion of solute between the particle and the interface on the particle pushing phenomena. *Acta Materialia*, 46(4):1115–1123, 1998.

[14] Adrian V. Catalina, Subhayu Sen, Doru M. Stefanescu, and William F. Kaukler. Interaction of porosity with a planar solid/liquid interface. *Metallurgical and Materials Transactions A*, 35(5):1525–1538, 2004.

[15] Sidhanth Tyagi, Hélène Huynh, Cécile Monteux, and Sylvain Deville. Objects interacting with solidification fronts: Thermal and solute effects. *Materialia*, 12(April):100802, 2020.

[16] Justin C. T. Kao and Alexander A. Golovin. Particle capture in binary solidification. *Journal of Fluid Mechanics*, 625(September 2008):299, 2009.

[17] Yi Yang, JW Garvin, and HS Udaykumar. Sharp interface numerical simulation of directional solidification of binary alloy in the presence of a ceramic particle. *International journal of heat and mass transfer*, 51(1-2):155–168, 2008.

[18] JS Wettlaufer and M Grae Worster. Premelting dynamics. *Annu. Rev. Fluid Mech.*, 38:427–452, 2006.

[19] Dmytro Dedovets, Cécile Monteux, and Sylvain Deville. Five-dimensional imaging of freezing emulsions with solute effects. *Science*, 360(6386):303–306, 2018.

[20] J. A. Sekhar and R. Trivedi. Solidification microstructure evolution in the presence of inert particles. *Materials Science and Engineering A*, 147(1):9–21, 1991.

[21] Jürgen Pötschke and Volker Rogge. On the behaviour of foreign particles at an advancing solid-liquid interface. *Journal of Crystal Growth*, 94(3):726–738, 1989.

[22] A. W. Rempel and M. G. Worster. Interaction between a particle and an advancing solidification front. *Journal of Crystal Growth*, 205(3):427–440, 1999.

30

[23] A. W. Rempel and M. G. Worster. Particle trapping at an advancing solidification front with interfacial-curvature effects. *Journal of Crystal Growth*, 223(3):420–432, 2001.

[24] Min S. Park, Alexander A. Golovin, and Stephen H. Davis. The encapsulation of particles and bubbles by an advancing solidification front. *Journal of Fluid Mechanics*, 560:415–436, 2006.

[25] P. S. Wei and S.Y. Y. Hsiao. Pore shape development from a bubble captured by a solidification front. *Int. J. Heat Mass Transf.*, 55(25-26):8129–8138, dec 2012.

[26] E. A. Ghezal, H. Li, A. Nehari, G. Alombert-Goget, A. Brenier, K. Lebbou, M. F. Joubert, and M. T. Soltani. Effect of pulling rate on bubbles distribution in sapphire crystals grown by the micropulling down (μ-PD) technique. *Crystal Growth and Design*, 12(8):4098–4103, 2012.

[27] H. Jamgotchian, R. Trivedi, and B. Billia. Interface dynamics and coupled growth in directional solidification in presence of bubbles. *Journal of Crystal Growth*, 134(3-4):181–195, 1993.

[28] S. Sen, W. F. Kaukler, P. Curreri, and D. M. Stefanescu. Dynamics of solid/liquid interface shape evolution near an insoluble particle - An X-ray transmission microscopy investigation. *Metallurgical and Materials Transactions A: Physical Metallurgy and Materials Science*, 28(10):2129–2135, 1997.

[29] F López Arbeloa, P Ruiz Ojeda, and I López Arbeloa. Flourescence self-quenching of the molecular forms of rhodamine b in aqueous and ethanolic solutions. *Journal of luminescence*, 44(1-2):105–112, 1989.

[30] Rex Malcolm Chaplin Dawson, Daphne C Elliott, William H Elliott, and Kenneth M Jones. *Data for biochemical research*, volume 3. Clarendon Press, 2002.

[31] Eleanor LV Harris, S Angal, and Simon Roe. *Protein purification applications: a practical approach*, volume 71. IRL press Oxford, 1990.

[32] Alan D McNaught, Andrew Wilkinson, et al. *Compendium of chemical terminology*, volume 1669. Blackwell Science Oxford, 1997.

[33] Johannes Schindelin, Ignacio Arganda-Carreras, Erwin Frise, Verena Kaynig, Mark Longair, Tobias Pietzsch, Stephan Preibisch, Curtis Rueden, Stephan Saalfeld, Benjamin Schmid, et al. Fiji: an open-source platform for biological-image analysis. *Nature methods*, 9(7):676, 2012.

[34] Stéfan van der Walt, Johannes L. Schönberger, Juan Nunez-Iglesias, François Boulogne, Joshua D. Warner, Neil Yager, Emmanuelle Gouillart, Tony Yu, and the scikit-image contributors. scikit-image: image processing in Python. *PeerJ*, 2:e453, 6 2014.

[35] Dmytro Dedovets, Cécile Monteux, and Sylvain Deville. A temperature-controlled stage for laser scanning confocal microscopy and case studies in materials science. *Ultramicroscopy*, 195(August):1–11, 2018.

[36] W. A. Tiller, K. A. Jackson, J. W. Rutter, and B. Chalmers. The redistribution of solute atoms during the solidification of metals. *Acta Metallurgica*, 1(4):428–437, 1953.

[37] JL Anderson, ME Lowell, and DC Prieve. Motion of a particle generated by chemical gradients. part 1. non-electrolytes. *J. Fluid Mech*, 117(1):107–121, 1982.

[38] Rodrigo Nery-Azevedo, Anirudha Banerjee, and Todd M Squires. Diffusiophoresis in ionic surfactant gradients. *Langmuir*, 33(38):9694–9702, 2017.

[39] Trevor J Shimokusu, Vanessa G Maybruck, Jesse T Ault, and Sangwoo Shin. Colloid separation by co2-induced diffusiophoresis. *Langmuir*, 36(25):7032–7038, 2019.

[40] Suin Shim and Howard A Stone. Co2-leakage-driven diffusiophoresis causes spontaneous accumulation of charged materials in channel flow. *Proceedings of the National Academy of Sciences*, 117(42):25985–25990, 2020.

[41] P. S. Wei, C.C. Huang, Z.P. Wang, K.Y. Chen, and C.H. Lin. Growths of bubble/pore sizes in solid during solidification—an in situ measurement and analysis. *J. Cryst. Growth*, 270(3-4):662–673, 2004.

[42] Norizaku Maeno. Air bubble formation in ice crystals. *Phys. Snow Ice Proc.*, 1(1):207–2181, 1967.

[43] P. S. Wei and C.Y Ho. An Analytical Self-Consistent Determination of a Bubble with a Deformed Cap Trapped in Solid during Solidification. *Metall. Mater. Trans. B*, 33(February):91–100, 2002.

[44] AA Chernov, DE Temkin, and AM Mel'Nikova. The influence of the thermal conductivity of a macroparticle on its capture by a crystal growing from a melt. *Sov. Phys. Crystallogr*, 22(6):656–658, 1977.

[45] R. Sasikumar and T. R. Ramamohan. Distortion of the temperature and solute concentration fields due to the presence of particles at the solidification front-effects on particle pushing. *Acta Metallurgica Et Materialia*, 39(4):517–522, 1991.

[46] J. Wettlaufer. Impurity Effects in the Premelting of Ice. *Physical Review Letters*, 82(12):2516–2519, 1999.

[47] A. W. Rempel, J. S. Wettlaufer, and M. G. Worster. Interfacial Premelting and the Thermomolecular Force: Thermodynamic Buoyancy. *Physical Review Letters*, 87(8):088501, 2001.

[48] Julia Schollick. *Real space study of pattern formation in freezing colloidal suspensions*. PhD thesis, University of Oxford, 2012.

[49] Navaneeth K. Marath and J. S. Wettlaufer. Impurity effects in thermal regelation. *Soft Matter*, 16(25):5886–5891, 2020.
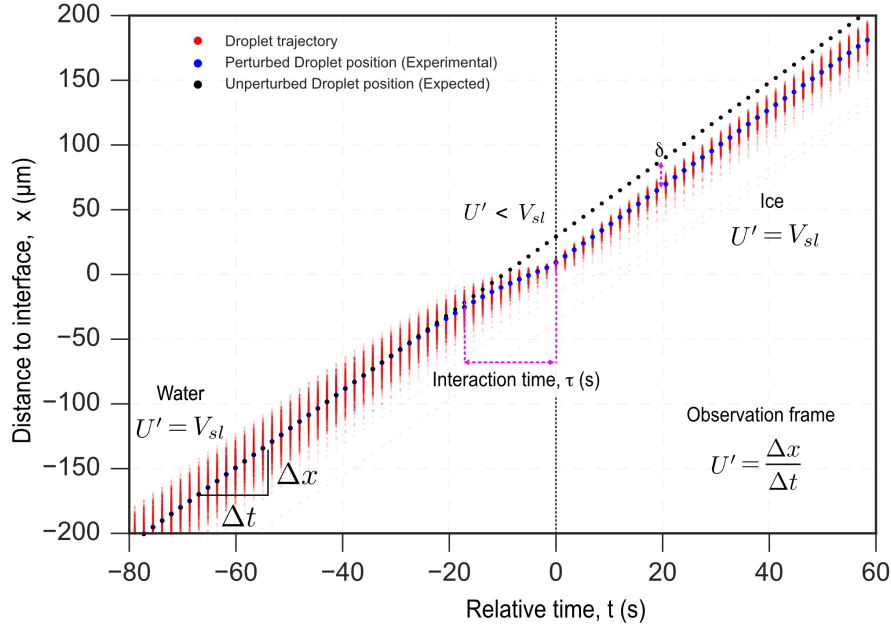
5   Supplementary Information

Figure S1: **Measurement of interaction time and apparent droplet velocity** U' **in the observation frame.** In the observation frame, far from the solid-liquid interface in water the droplet moves at the imposed growth rate $U' = V_{sl}$, as the droplet approaches the interface it gets repelled $U' \neq V_{sl}$, and as the droplet is engulfed in the ice it doesn't get repelled anymore, thereby recovering $U' = V_{sl}$. The interaction time is the total duration over which a droplet gets repelled by the solidification interface. Relative time is zero when the front edge of the droplet hits the solidification front. Experimental conditions for which the curve was recorded: $V_{sl} = 3\ \mu m \cdot s^{-1}$, $G = \nabla T = 10^4\ K \cdot m^{-1}$, Droplet size $R_1 = 7.2 \pm 0.4\ \mu m$.
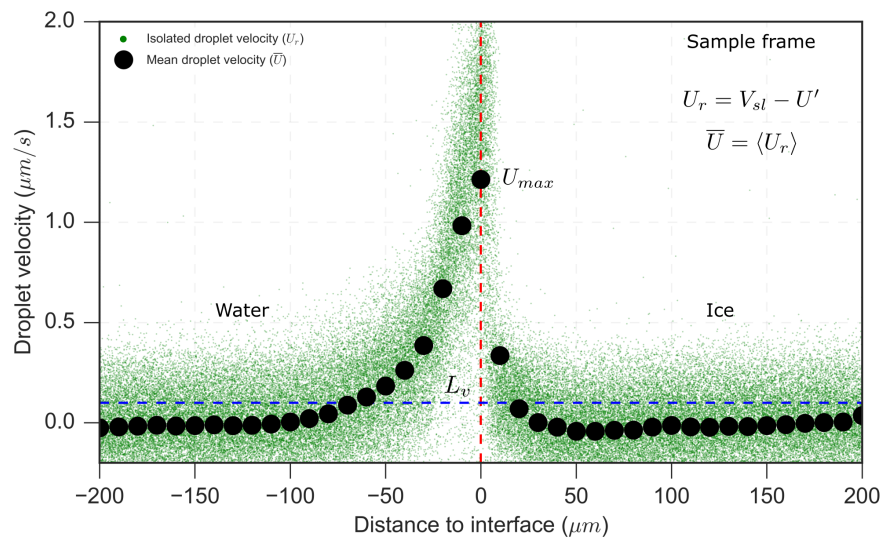
Figure S2: **Deducing the isolated droplet velocity U_r and the mean droplet velocity $\overline{U}$ in the sample frame.** In the sample frame, the isolated droplet velocity U_r is zero far from the interface, it increases and reaches a maximum when the droplet gets repelled by the interface and subsequently, reduces to zero as the droplet is engulfed in the ice. Experimental conditions for which the curve was recorded: $V_{sl} = 3\ \mu m \cdot s^{-1}$, $G = \nabla T = 10^4\ K \cdot m^{-1}$, Droplet size $R_1 = 7.2 \pm 0.4\ \mu m$. $^{\copyright}$ (2020) S. Tyagi *et al.* (10.6084/m9.figshare.14815083) CC BY 4.0 license https://creativecommons.org/licenses/by/4.0/.